European Radiology (2019) 29:4812–4821
https://doi.org/10.1007/s00330-018-5966-1

NUCLEAR MEDICINE

Does whole-body Patlak ^{18}F-FDG PET imaging improve lesion detectability in clinical oncology?

Guillaume Fahrni[1] · Nicolas A. Karakatsanis[2] · Giulia Di Domenicantonio[1] · Valentina Garibotto[1,3] · Habib Zaidi[1,4,5,6]

Received: 27 August 2018 / Revised: 7 November 2018 / Accepted: 11 December 2018 / Published online: 28 January 2019

Abstract

Purpose Single-pass whole-body (WB) ^{18}F-FDG PET/CT imaging is routinely employed for the clinical assessment of malignant, infectious, and inflammatory diseases. Our aim in this study is the systematic clinical assessment of lesion detectability in multi-pass WB parametric imaging enabling direct imaging of the highly quantitative ^{18}F-FDG influx rate constant K_i, as a complement to standard-of-care standardized uptake value (SUV) imaging for a range of oncologic studies.

Methods We compared SUV and K_i images of 18 clinical studies of different oncologic indications (lesion characterization and staging) including standard-of-care SUV and dynamic WB PET protocols in a single session. The comparison involved both the visual assessment and the quantitative evaluation of SUV_{mean}, SUV_{max}, K_{imean}, K_{imax}, tumor-to-background ratio (TBR_{SUV}, TBR_{Ki}), and contrast-to-noise ratio (CNR_{SUV}, CNR_{Ki}) quality metrics.

Results Overall, both methods provided good-quality images suitable for visual interpretation. A total of 118 lesions were detected, including 40 malignant (proven) and 78 malignant (unproven) lesions. Of those, 111 were detected on SUV and 108 on K_i images. One proven malignant lesion was detected only on K_i images whereas none of the proven malignant lesions was visible only on SUV images. The proven malignant lesions had overall higher K_i TBR and CNR scores. One unproven lesion, which was later confirmed as benign, was detected only on the SUV images (false-positive). Overall, our results from 40 proven malignant lesions suggested improved sensitivity (from 92.5 to 95%) and accuracy (from 90.24 to 95.12%) and potentially enhanced specificity with K_i over SUV imaging.

Conclusion Oncologic WB Patlak K_i imaging may achieve equivalent or superior lesion detectability with reduced false-positive rates when complementing standard-of-care SUV imaging.

Key Points

- *The whole-body spatio-temporal distribution of ^{18}F-FDG uptake may reveal clinically useful information on oncologic diseases to complement the standard-of-care SUV metric.*
- *Parametric imaging resulted in less false-positive indications of non-specific ^{18}F-FDG uptake relative to SUV.*
- *Parametric imaging may achieve equivalent or superior ^{18}F-FDG lesion detectability than standard-of-care SUV imaging in oncology.*

Keywords Positron emission tomography · Molecular imaging · Tumors

Electronic supplementary material The online version of this article (https://doi.org/10.1007/s00330-018-5966-1) contains supplementary material, which is available to authorized users.

✉ Nicolas A. Karakatsanis
nak2032@med.cornell.edu

✉ Habib Zaidi
habib.zaidi@hcuge.ch

[1] Division of Nuclear Medicine and Molecular Imaging, Geneva University Hospital, CH-1211 Geneva, Switzerland

[2] Division of Radiopharmaceutical Sciences, Department of Radiology, Weill Cornell Medical College of Cornell University, New York, NY 10021, USA

[3] Faculty of Medicine, University of Geneva, 1205 Geneva, Switzerland

[4] Geneva University Neurocenter, University of Geneva, 1205 Geneva, Switzerland

[5] Department of Nuclear Medicine and Molecular Imaging, University of Groningen, 9700 RB Groningen, Netherlands

[6] Department of Nuclear Medicine, University of Southern Denmark, DK-500 Odense, Denmark

Abbreviations

^{18}F-FDG	^{18}F-Fluorodeoxyglucose
CT	Computed tomography
FOV	Field-of-view
IDIF	Image-derived input function
LV	Left ventricle
PET	Positron emission tomography
PET/CT	Positron emission tomography/computed tomography
ROI	Region of interest
SUV	Standardized uptake value
TOF	Time-of-flight
VOI	Volume of interest
WB	Whole-body

Introduction

Whole-body (WB) ^{18}F-FDG PET/CT imaging is widely used in clinical oncology for multiple indications, including lesion characterization, staging, restaging, and therapy monitoring [1, 2]. In current clinical practice, oncologic PET/CT exams mainly consist of scans performed across multiple bed positions over a single time period or frame at late time points, when equilibrium is reached. The acquired data are then averaged over the acquisition time frame and reconstructed to produce conventional (static) PET images. The images are quantified in units of standardized uptake value (SUV), which serve as a surrogate of static metabolic activity normalized to the body weight and the administered tracer dosage [3]. Yet, SUV remains a semi-quantitative index subject to a large variability due to several factors related to the scanning procedure or the patient's physiology, such as patient's body composition, plasma glucose level, time between injection and measurement, and duration of the scan time frame [4]. Moreover, static imaging is unable to provide information about the kinetics of ^{18}F-FDG in the regions of interest [5].

The dynamic course of the ^{18}F-FDG spatial distribution in the targeted tissues may reveal highly useful clinical information on tissue's metabolic properties, such as the metabolic rate of glucose uptake post ^{18}F-FDG injection. These image metrics could, in turn, facilitate tumor characterization and therapy response assessment [6–9]. For this reason, dynamic PET imaging techniques were also introduced allowing the scanning of a limited axial field-of-view (single bed position) over time to enable the extraction of important tracer kinetic parameters, such as the uptake rate. The tracer kinetic parameters were initially estimated on a region level by averaging the dynamic PET images within specific volumes of interest (VOIs) [10, 11]. Later, larger computational resources allowed for voxel-wise estimation of the tracer kinetic parameters at the cost of higher noise levels, thus leading to parametric imaging [12]. Despite the potential for better lesion detectability and reduced rate of false positives [13], dynamic and parametric imaging has hitherto been limited to research setting and single-bed field-of-views (FOVs) [14–16].

Different strategies were developed for the generation of parametric images, ranging from streamlined graphical analysis, such as the Patlak method [17], to spectral analysis [18] and to the most complex full compartmental modeling methods [19]. Although the two latter techniques are more informative, they can be unstable, sensitive to statistical noise, and difficult to adopt in the clinic, due to the large number of fitting parameters and the high order of the associated kinetic models. In this regard, graphical analysis can be a simpler, yet robust, alternative approach enabling the direct estimation of the primary kinetic macro-components of the tracer uptake across multiple-bed FOVs.

However, WB dynamic PET acquisitions present the additional challenge of segmenting a given dynamic scan period across multiple bed positions, thereby inevitably introducing time gaps in between the time frames, which reduce the signal-to-noise ratio [20]. Nevertheless, recent technological advances in commercial clinical PET scanners, such as the use of longer axial FOVs [21], time-of-flight (TOF) information [22], and resolution modeling [23], allowed significant enhancement of the noise-equivalent count rate and sensitivity. In fact, the first introduced framework of WB dynamic ^{18}F-FDG PET/CT clinical imaging involved a 6-min dynamic acquisition over the heart bed, followed by four or six dynamic PET passes across multiple beds, and was successfully applied on a pilot cohort of oncology cases demonstrating its clinical feasibility [24–27]. The utilization of just two time frame acquisitions (passes) per bed position has also been reported [28]. Nevertheless, the use of six WB passes demonstrated improved performance, in terms of noise and bias, for the WB parametric images to enable the combined estimation of SUV and multiparametric PET images in a single scan session [29].

In this work, we systematically compare lesion detectability between Patlak and SUV ^{18}F-FDG WB clinical PET images, as extracted from the same cohort of oncologic patients. Our ultimate aim is to assess any benefits in WB ^{18}F-FDG lesion detectability by utilizing Patlak-based glucose metabolism metrics.

Materials and methods

Patient population

This is a prospective pilot study to facilitate the development of a noninvasive quantitative assessment strategy for dynamic whole-body ^{18}F-FDG oncologic PET imaging. We included adult patients who were referred for staging or restaging of lung or abdominal lesions by ^{18}F-FDG PET/CT. The

institutional ethics committee approved this study and all patients gave informed consent.

Data acquisition and image reconstruction

PET/CT scans were performed on a Siemens Biograph™ mCT scanner following injection of a standard dose of 3.5 MBq/kg (3.71 ± 1.05 MBq/kg) of ^{18}F-FDG. The patients underwent a scanning protocol of about 80 min consisting of the following (Fig. 1): (i) a low-dose CT for attenuation correction; (ii) a 6-min dynamic single-bed PET acquisition centered in the heart region for extrapolation of the input function (IF), starting simultaneously with the ^{18}F-FDG injection; (iii) a subsequent set of 13 whole-body PET scans in continuous bed motion (CBM) of about 3 min each; (iv) a subsequent SUV WB CBM scan of about 20 min used as a reference for comparison was acquired at the standard-of-care scan time window for ^{18}F-FDG studies (starting 60 min post-injection); and (v) a contrast-enhanced CT scan (13/18 patients) or a non-enhanced CT scan when contraindicated (i.e., renal failure).

All images were reconstructed using 3D iterative OSEM algorithm and parameters used in the clinic (2 iterations and 21 subsets), including TOF and resolution modeling [30], with a post-reconstruction Gaussian filter of 2 mm FWHM.

Methodology for whole-body parametric imaging

The Patlak graphical analysis utilized by the employed multi-pass WB parametric imaging framework is based on an irreversible two-tissue compartment kinetic model: ^{18}F-FDG in the blood plasma is reversibly absorbed (intra-cellular) by specific tissues in a free non-metabolized state (first tissue compartment) and then, unlike standard glucose, is irreversibly metabolized or phosphorylated (second compartment) into ^{18}F-FDG6P [31]. The exchanges between the compartments are modeled by the micro-parameters K_1 (plasma to non-phosphorylated compartment), k_2 (non-phosphorylated to plasma compartment), and k_3 (non-phosphorylated to phosphorylated compartment) rate constants. A zero efflux (dephosphorylation) rate constant ($k_4 = 0$) between the phosphorylated and the non-phosphorylated compartments is assumed. FDG k_4 parameter is widely assumed to be negligible and can be considered to be zero for the majority of tissues (k_4 may be positive in some regions, such as the liver, but its effect on the data is negligible for the early uptake phase). All the exchanges between the different compartments can be resumed in the ^{18}F-FDG macro-parameter of K_i, denoting the net uptake or influx rate constant:

$$Ki = \frac{K_1 k_3}{k_2 + k_3} \quad (1)$$

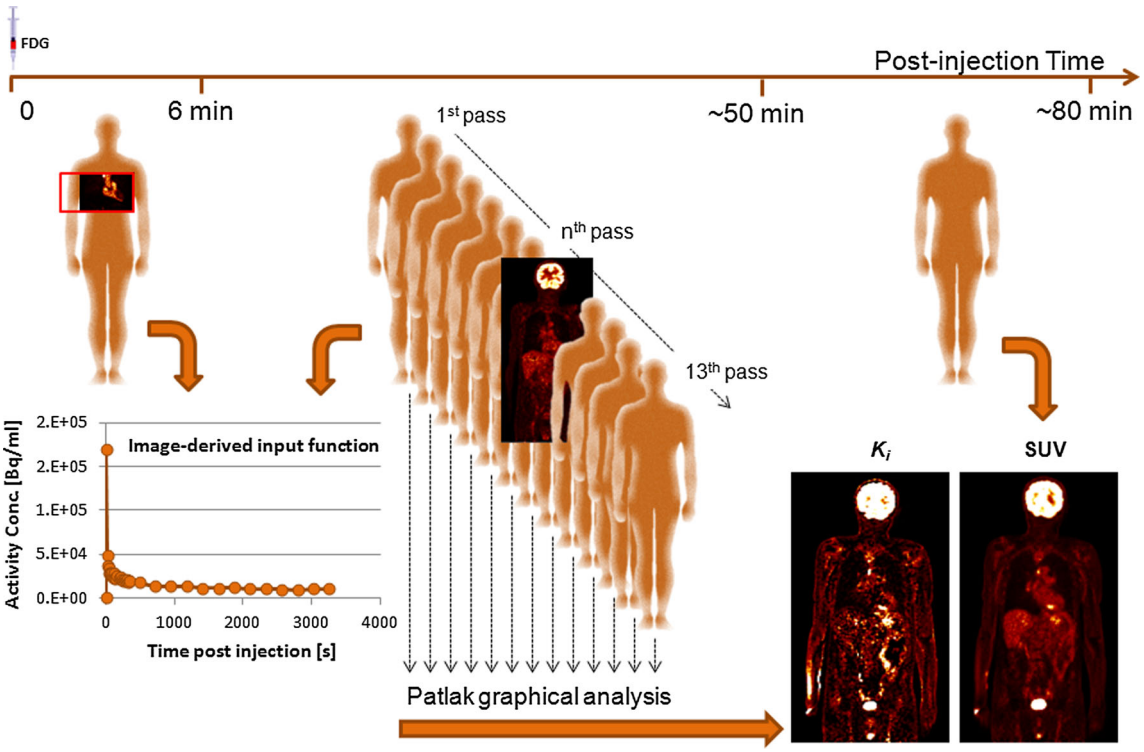

Fig. 1 Illustration of the whole-body PET/CT scanning protocol. The first dynamic acquisition is centered in the heart region to obtain the image-derived input function; the following 13 WB passes are acquired in CBM mode in the same axial FOV as the subsequent SUV acquisition. In a standard static PET WB protocol, the patient has to wait in a quiet place in order for the tracer uptake to be optimal for SUV imaging. Here, we use this idle time to perform the dynamic passes

In the assumption of irreversible trapping of the tracer, K_i can be directly estimated using the standard Patlak analysis on a voxel-by-voxel basis, resulting in K_i parametric maps [17]. We generated such K_i images by implementing an in-house MATLAB code (MathWorks Inc.). The tissue activity, $C(t)$, is linked to blood plasma time-activity concentration or input function (IF), $C_p(t)$, via the standard Patlak model linear equation:

$$C(t) = Ki\int_0^t Cp(t)dt + VCp(t) \quad (2)$$

where K_i and V are the uptake rate defined in Eq. 1 and the total blood plasma distribution volume, respectively. The activity in each tissue voxel $C(t)$ and the $C_p(t)$, as measured over time t from the dynamic PET images, are then fitted to the Patlak model equation to estimate via ordinary least squares regression the K_i and V parameters at every voxel.

In this protocol, $C(t)$ is sampled 13 times (once per pass) for each voxel; the $C_p(t)$ is determined using both the initial dynamic acquisition and the 13 passes. Finally, the parametric K_i images are normalized to the maximum SUV of the respective static scan to display the images on the same scale, thus facilitating head-to-head clinical interpretation and image comparison.

Derivation of the input function

The image-derived IF (IDIF) $C_p(t)$ is obtained from a region of interest (ROI) drawn in the left ventricle (LV) of the heart on images from both scans (ii) and (iii): the former was sampled in 12 frames of 10 s followed by 12 frames of 20 s, while a single IDIF value was obtained from the cardiac bed frame of each of the 13 WB passes.

A number of studies reported that the IDIF can also be extracted from the aorta rather than the left ventricle [32]. Therefore, we evaluated the difference between LV and aortic IDIF for two patients where arterial blood sampling was also performed as the gold standard IF. Comparable LV and aortic IDIFs were found, although both underestimated the gold standard IF at the peak (Fig. 2, left panel) and overestimated it at later times. However, the integral of the IF (Fig. 2, right panel), which is the only IF metric considered in Patlak analysis, varied by less than 5% in between LV, aortic, and gold standard IF resulting in minimal impact on the derived parametric images.

Image analysis

Visual interpretation SUV and K_i images were evaluated qualitatively on a dedicated workstation by two physicians (having only access to the clinical indication) who independently analyzed both images in two different and distant sessions followed by consensus reading and the writing of a single report for each set of images summarizing the findings. The overall quality of PET images was rated using a 5-point scale from 1 (inacceptable) to 5 (excellent) on the basis of the subjective impression of the overall quality of the PET data fused on the corresponding CT images, taking into account the impression of smoothness, resolution, sharpness of contours, noise, homogeneity, and presence of artifacts. A single consensual score was assigned by expert physicians. Inter-observer evaluation and comparison of different groups of readers are beyond the scope of this work. Both reports were then compared. Image quality was assessed as adequate/inadequate for visual reading and all primary tumors and other distant lesions, such as metastases, lymph nodes, or inflammatory uptake, were identified and quantitatively evaluated. We also included malignant (biopsy proven)/malignant (unproven) lesions that were not visible on either SUV or K_i images, but only on the CT component of the PET/CT examination accounting for the probability that lesions seen on CT but not on PET may be non-malignant. When possible, malignancy was confirmed by histology or other clinical indications provided in patient's follow-up.

We analyzed separately biopsy-proven or previously known lesions, which were classified as proven malignant, from lesions considered as unproven malignant with high clinical probability for malignancy (i.e., new lesions in a patient with metastases or lesions confirmed on contrast-enhanced CT in case of FDG-non avid lesions, such as hepatocellular carcinoma (HCC)). In cases where a significant number of lesions was identified in the same organ or anatomical region (i.e., multiple abdominal lymph nodes), a maximum of 5 lesions were analyzed to reduce bias.

Quantitative analysis A 3D ROI was manually drawn on each lesion to estimate at the same position the SUV_{max} and K_{imax} metrics. When the lesions were non-metabolic, the ROIs were drawn on the contrast-enhanced CT images. Background ROI mean, BKG_{mean}, and standard deviation, BKG_{sd}, metrics were extracted from the same positions, between SUV and K_i images, in healthy surrounding tissues. Tumor-to-background ratio (TBR) and contrast-to-noise ratio (CNR) scores were then calculated as defined in Eqs. 3 and 4.

$$\mathrm{TBR} = (\text{Tumor ROI}_{max}/\text{Background ROI}_{mean}) - 1 \quad (3)$$

$$\mathrm{CNR} = \mathrm{TBR}/\text{Background ROI}_{SD} \quad (4)$$

Finally, all identified lesions were regrouped in organs regardless of the origin of the lesion (primary tumor, metastases, malignant (unproven) lesion).

Statistical analysis

Spearman's rank correlation coefficient (ρ) was used to assess the correlation between SUV_{max} and K_{imax} of all lesions as

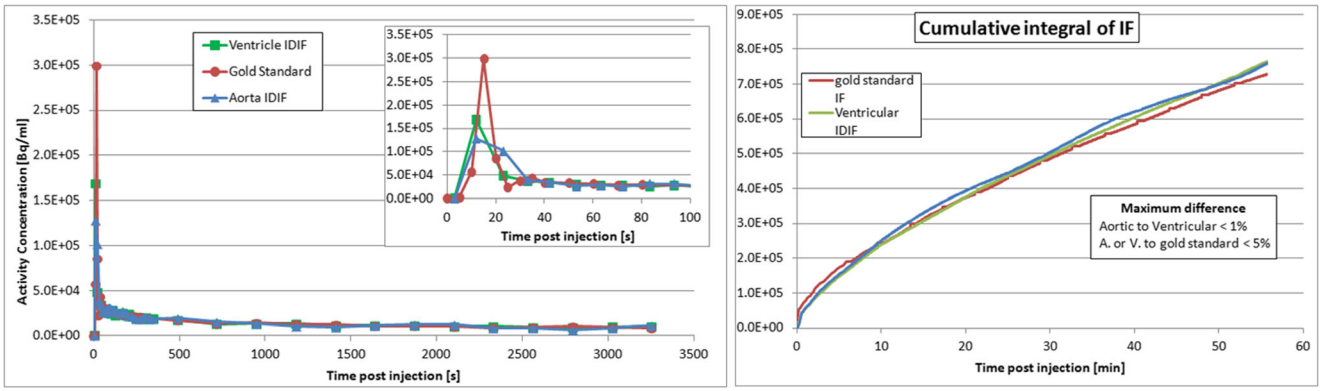

Fig. 2 Input functions obtained from image ROIs drawn on heart LV (green) and aorta (blue) ROIs, as well as from arterial blood sampling (red). The inset in the left panel shows a zoom of the peak region. The right panel shows the cumulative integral of the IFs shown on the left

well as between background values. A p value < 0.01 was considered significant for this test. A Wilcoxon signed-rank test was performed to assess the statistical significance of the differences between TBR_{Ki} and TBR_{SUV} and between CNR_{Ki} and CNR_{SUV} for the 40 malignant lesions. A p value < 0.05 was considered significant for this test.

Results

Eighteen patients originally scheduled for an oncologic whole-body ^{18}F-FDG PET/CT (6 females and 12 males; mean age = 58.8 ± 16.8 years) were enrolled. A description of the cohort, including the indication for the study and the number and location of detected lesions, is reported in Table 1. Both modalities produced good-quality images adequate for visual interpretation. The qualitative inspection of the PET images by expert physicians suggested similar (or lower) image quality for the K_i (4.05), relative to SUV (4.2) images. However, the K_i image quality absolute scores were acceptable, the only discordant case being one patient with significant bulk motion during the long dynamic WB scan. The most notable visual difference, as illustrated in Fig. 3, was the suppression of the blood compartment in K_i images, particularly for organs with a non-negligible blood pool component, such as the liver, the spleen, and the blood vessels (Table 2), resulting in a higher contrast for individual lesions. This is in agreement with previous studies [24–27]. A total of 118 biopsy-proven malignant ($n = 40$) or unproven malignant ($n = 78$) lesions were identified and analyzed.

Of the 40 confirmed malignant lesions, 37 (93%) were detected on SUV and 38 (95%) on K_i images. The malignant lesions have higher K_i TBR ($p < 0.001$) and CNR ($p < 0.001$) scores. The 2 lesions not detected on both modalities were HCC nodules on the same patient (patient no. 18), appearing as non-hypermetabolic. Those two lesions were not detected on K_i images despite their high TBR and CNR scores, which may be attributed to the very low K_i values, as discussed later. The only lesion detected with K_i but not with SUV images was a hepatic lesion (patient no. 1, Fig. 3), a 71-year-old male presenting a suspicious liver mass, described as hypervascular on the contrast-enhanced CT examination. The standard report of the SUV images described the lesion as non-metabolic (SUV_{max} 4.45, BKG_{mean} 2.2, TBR 1.02, CNR 2.82), whereas it was described as hypermetabolic in the report generated from the K_i images (K_{imax} 1.43, BKG_{mean} 0.24, TBR 5.37, CNR 29.17). Biopsy later confirmed the lesion to be a HCC.

Of the 78 unproven malignant lesions, 74 (95%) were detected with SUV images whereas 70 (90%) of them were detected on K_i images. The four lesions not detected on either modality were non-hypermetabolic liver lesions (patient no. 2 and no. 12) suspected as HCC nodules on the basis of CT and MR imaging, but never proven with a biopsy. The four lesions not detected on K_i images only were the following: a hypermetabolic focal sigmoid activity (patient no. 10); a slightly hypermetabolic lymph node (patient no. 14); a slightly hypermetabolic focal brain activity (patient no. 14); and a lung lesion (patient no. 8, Fig. 4). The first three lesions were not confirmed as either malignant or benign during the follow-up. The last lesion was a false-positive case of a 54-year-old male with a suspicious left lung lesion, confirmed as benign at biopsy. The standard report of the SUV images described the lesion as hypermetabolic (SUV_{max} 1.5, BKG_{mean} 0.29, TBR 4.17, CNR 81.81), whereas it was not detected in the report generated from the K_i images (K_{imax} 0.47, BKG_{mean} 0.02, TBR 22.5, CNR 2812.5).

Considering the biopsy results as our gold standard outcome for assessing malignancy of lesions, we assessed the sensitivity and accuracy for the 40 lesions proven as malignant. In this group of lesions, the sensitivity in detecting malignancy increased from 37 × 100 40 = 92.5%, in the case of SUV, to 38 × 100 40 = 95%, in the case of K_i imaging. As we only had one biopsy-confirmed negative lesion, we cannot reliably compare the specificity performance between SUV and K_i imaging. Nevertheless, we were able to

Table 1 Clinical characteristics of the patients' population and summary of the lesions detected

Patient	Age	Sex	Malignancy	Detected lesions
1	71	M	Hepatocellular carcinoma	Liver (1)
2	70	M	Pancreatic adenocarcinoma	Pancreas (1), liver (2), lymph nodes (1)
3	69	M	Pancreatic adenocarcinoma	Pancreas (1), lymph nodes (4)
4	42	M	Neuroendocrine carcinoma	Lungs (1), subcutaneous tissue (1), lymph nodes (2)
5	59	M	Hepatocellular carcinoma	Liver (1), lymph nodes (3)
6	67	M	Lung epidermoid carcinoma	Lungs (1)
7	58	M	Rectum adenocarcinoma	Colon (3), lungs (2), subcutaneous tissue (5), peritoneum (5), lymph nodes (3), liver (3), muscles (1)
8	54	M	Suspicious lung lesion	Lungs (1)
9	64	M	Melanoma	Lungs (1), liver (2)
10	56	F	Lung carcinoid	Lungs (1), colon (1)
11	42	F	Lung adenocarcinoma	Lungs (2), lymph nodes (3)
12	74	M	Intrahepatic cholangiocarcinoma	Liver (3), lymph nodes (5), brain (1)
13	45	F	Hepatic adenocarcinoma	Liver (6), lungs (2), colon (2), bones (5), lymph nodes (8)
14	45	F	Gastric adenocarcinoma	Stomach (1), lymph nodes (3), bones (2), brain (1)
15	62	F	Lung adenocarcinoma	Lungs (1), colon (1)
16	59	F	Lung neuroendocrine carcinoma	Lungs (1), adrenal gland (3), bones (1), lymph nodes (4)
17	60	M	Lung Hodgkin lymphoma	Lungs (1), bones (1), lymph nodes (11)
18	61	M	Hepatocellular carcinoma	Liver (2), parotid gland (1)

correctly assess this single true-negative indication only with K_i imaging, therefore suggesting improved specificity with K_i imaging. As a result, our accuracy in detecting malignancy was further improved from $37 \times 100 \quad 41 = 90.24\%$ with SUV to $39 \times 100 \quad 41 = 95.12\%$ with K_i imaging.

PET metrics and statistical analysis

Spearman's rank correlation coefficient (ρ), which was calculated independently of the anatomical region, was 0.777 ($p < 0.001$) for $K_{i\text{max}}$-SUV_{max} of all lesions and 0.414 ($p < 0.001$) for $K_{i\text{mean}}$-

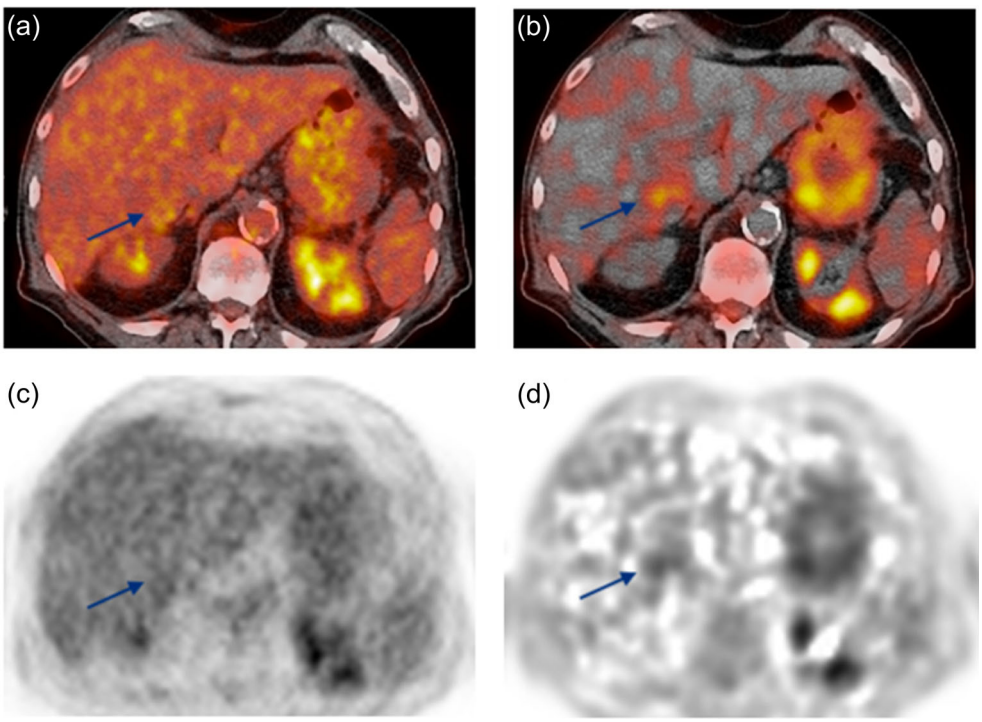

Fig. 3 Case of a hepatocellular carcinoma (patient no. 1) appearing as non-metabolic in the SUV images and as hypermetabolic in the K_i images, later confirmed with biopsy as hepatocellular carcinoma. **a** SUV fused with non-contrast abdomen CT, **b** K_i fused with non-contrast abdomen CT, **c** SUV images, and **d** K_i images. Note how the surrounding, normal liver tissue is less visible on K_i images, but with a noisier aspect

Table 2 Typical SUV and normalized K_i values for normal tissue in different organs

	SUV range (mean ± SD)	K_i (normalized) range (mean ± SD)
Thoracic vertebra	1.10–2.56 (1.88 ± 0.37)	0.11–2.63 (0.70 ± 0.55)
Lung	0.19–0.76 (0.38 ± 0.16)	$4{\cdot}10^{-3}$–0.43 (0.12 ± 0.15)
Blood pool	1.21–2.48 (1.75 ± 0.34)	0–0.45 (0.14 ± 0.16)
Liver	1.47–3.05 (2.15 ± 0.38)	0–2.88 (0.55 ± 0.70)
Muscle	0.10–0.91 (0.61 ± 0.17)	0.017–1.40 (0.31 ± 0.33)

SUV_{mean} of all background regions. Table 3 and Fig. 6 show the correlations for each anatomical region.

TBR_{SUV} values ranged from 0.32 to 59.26, whereas TBR_{Ki} values ranged from 2.6 to 9229. TBR_{Ki} values were higher than TBR_{SUV} values for 38 lesions out of 40 (95%). The Wilcoxon signed-rank test showed statistically significant differences between the two metrics ($p < 0.001$). CNR_{SUV} values ranged from 1.08 to 2693.78, whereas CNR_{Ki} values ranged from 1.82 to 2,307,250. CNR_{Ki} values were higher than CNR_{SUV} values for 33 lesions out of 40 (82.5%). The Wilcoxon signed-rank test showed statistically significant differences between the two metrics ($p < 0.001$).

Multiple findings of muscle focal activity, non-suspicious lymph nodes, digestive metabolism, or other similar foci presumably benign were visible on SUV images but negative on K_i images. As an example of such findings, we report a case of a 45-year-old female (patient no. 14, Supplementary Fig. 1) presenting with a gastric adenocarcinoma. The SUV image report described a non-suspicious thoracic lymph node (SUV_{max} 3.34, BKG_{mean} 2.6, TBR 0.28, CNR 0.31), which was not documented on the K_i image report (K_{imax} 0.73, BKG_{mean} 0.55, TBR 0.33, CNR 0.64).

Discussion

This study demonstrated that multi-pass whole-body PET K_i parametric imaging, utilizing robust Patlak graphical analysis, may achieve equivalent or, potentially, superior lesion detectability than standard-of-care SUV imaging with reduced false-positive rates in routine oncology applications. The implemented protocol generated both static SUV and parametric K_i images in a single session, thereby allowing for reliable and objective comparisons between the two modalities. In our study, all produced images were of good quality with all biopsy proven malignant lesions visible in SUV images also depicted in K_i images. However, K_i images proved superior in three situations: one proven malignant lesion only being detected on K_i images, as well as one false-positive lesion and a benign lymph node being positive only in SUV images. A major finding of our work is the

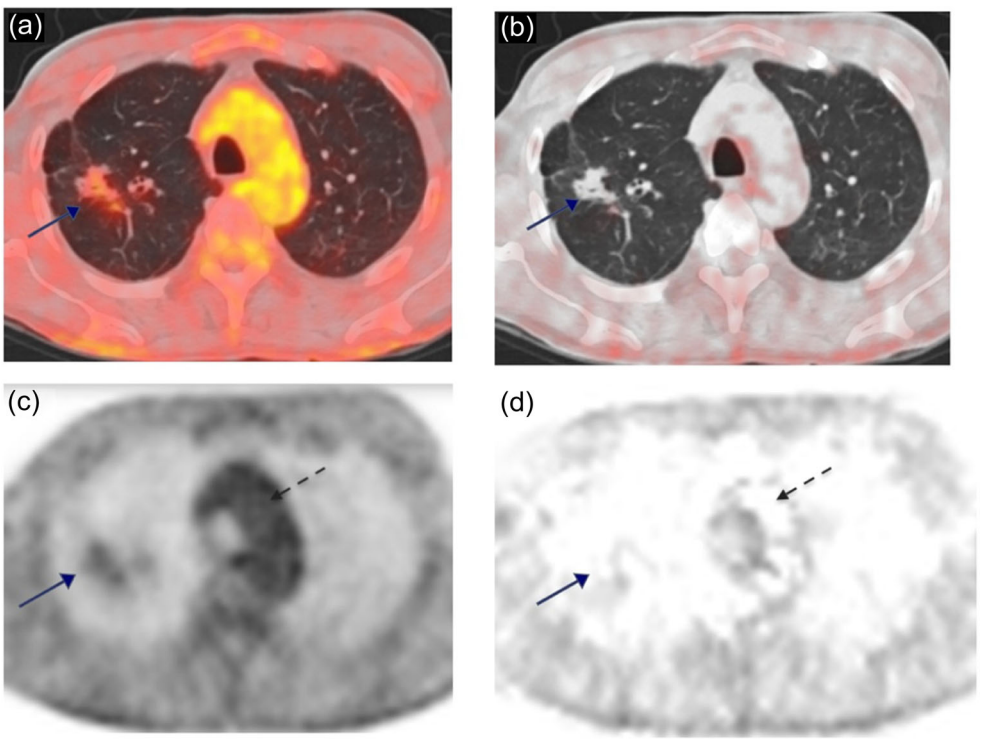

Fig. 4 Case of an inflammatory lung lesion (patient no. 8), initially declared as malignant (unproven) in the standard SUV report, confirmed benign by biopsy during the follow-up. This lesion was declared as benign in the K_i report. **a** SUV fused with non-contrast abdomen CT, **b** K_i fused with non-contrast abdomen CT, **c** SUV images, and **d** K_i images. Note the very different aspect of the arch of the aorta (dashed arrow) on both modalities suggesting suppression of blood pool signal in the K_i images

Table 3 Spearman's correlation (ρ) and p values (Sig. 2-tailed) between SUV and K_i images, calculated for the maximum values of the lesions and the mean values of the backgrounds. Correlation is deemed significant for $p < 0.01$. All values are reported for the full dataset and for lesions grouped by localization

	Spearman's ρ lesions	Spearman's ρ background
Total	0.777 ($p < 0.001$)	0.414 ($p < 0.001$)
Abdominal	0.796 ($p < 0.001$)	0.923 ($p < 0.001$)
Liver	0.890 ($p < 0.001$)	− 0.324 ($p = 0.164$)
Lungs	0.780 ($p = 0.001$)	0.252 ($p = 0.385$)
Bones	0.950 ($p < 0.001$)	0.875 ($p = 0.002$)
Lymph nodes	0.657 ($p < 0.001$)	− 0.018 ($p = 0.904$)
Other	0.806 ($p = 0.005$)	0.517 ($p = 0.126$)

suppression of the non-specific ^{18}F-FDG signal in the blood compartments allowing for a higher contrast in abnormal uptake regions, thereby confirming observations made in previous studies [24–27, 33]. This observation suggests increased likelihood of detecting metabolically active lesions surrounded by avid background non-specific uptake, such as in the case of intermediate differentiated HCCs with ^{18}F-FDG imaging.

The Patlak graphical approach is of low linear complexity, thus allowing for fast computation and wide adoptability of WB parametric PET imaging in clinical practice. On the other hand, it assumes an irreversible ^{18}F-FDG uptake, a condition not always satisfied in normal liver, kidneys, and certain tumors, such as HCCs [34], thereby leading to K_i underestimation. Thus, an extended non-linear generalized Patlak model, considering a mild degree of reversibility, had been previously proposed [26] and could be easily integrated in our analysis. However, the use of a standard linear graphical analysis model is more preferable, thanks to its robustness to data noise, when the kinetic parameters are indirectly estimated from the dynamic PET images, and higher lesion contrast, when K_i is underestimated only in the background.

We found a strong positive correlation ($\rho = 0.791$) between $K_{i\max}$ and SUV_{max}, and even stronger correlations when looking separately at different organs. This suggests that K_i images will identify hypermetabolic lesions if these are depicted on SUV images. In background neighboring regions, however, we found weak positive correlations ($\rho = 0.392$) between BKG_{mean}-K_i and BKG_{mean}-SUV, which is expected owing to blood pool suppression within K_i images.

The TBR and CNR are almost always higher in K_i images (Fig. 5). On a purely visual examination, most of the malignant lesions were depicted on both modalities, except two HCC nodules appearing as non-hypermetabolic on both modalities and one HCC only depicted on K_i images. Thus, in the majority of cases, the TBR_{SUV} was largely sufficient to detect the lesions.

In the case of the lung lesions, for example, where the highest TBR values were found, we observe that most lung lesions are associated with a very low metabolism, resulting in lung lesions being easily detected. Overall, a TBR value between 3 and 5 is generally adequate in differentiating the lesion from its background, if the lesion has sufficient metabolic activity. Therefore, improving the TBR beyond this range with parametric imaging will not further improve lesion detectability, although it may improve quantification. On the other hand, detectability may be challenging for lesions with low TBR_{SUV} scores especially within a highly vascularized organ of high BKG_{mean} uptake, such as the liver. Detectability may then be improved by the higher TBR_{Ki}, due to suppression of the background signal. An example for such case is the

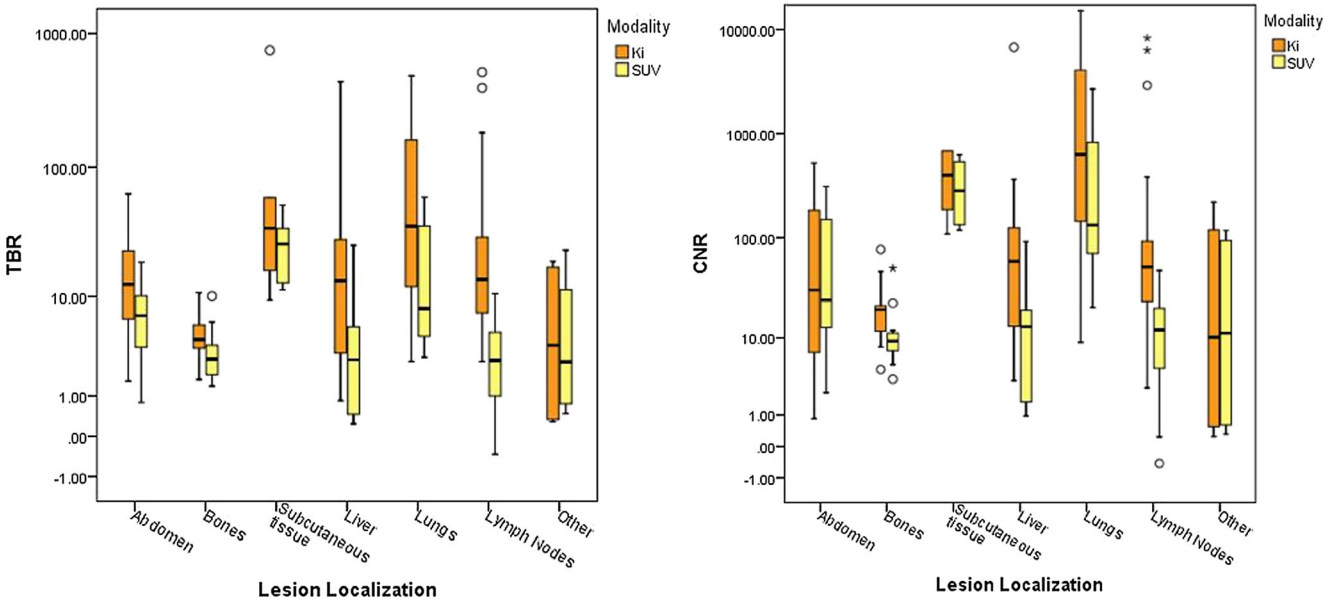

Fig. 5 Whisker plots showing TBR and CNR for the SUV and K_i images, presented by organ. Ki_{TBR} values are always higher than SUV_{TBR} values, regardless of the anatomical region, although the difference is variable depending on the organ. The same finding is observed for CNR

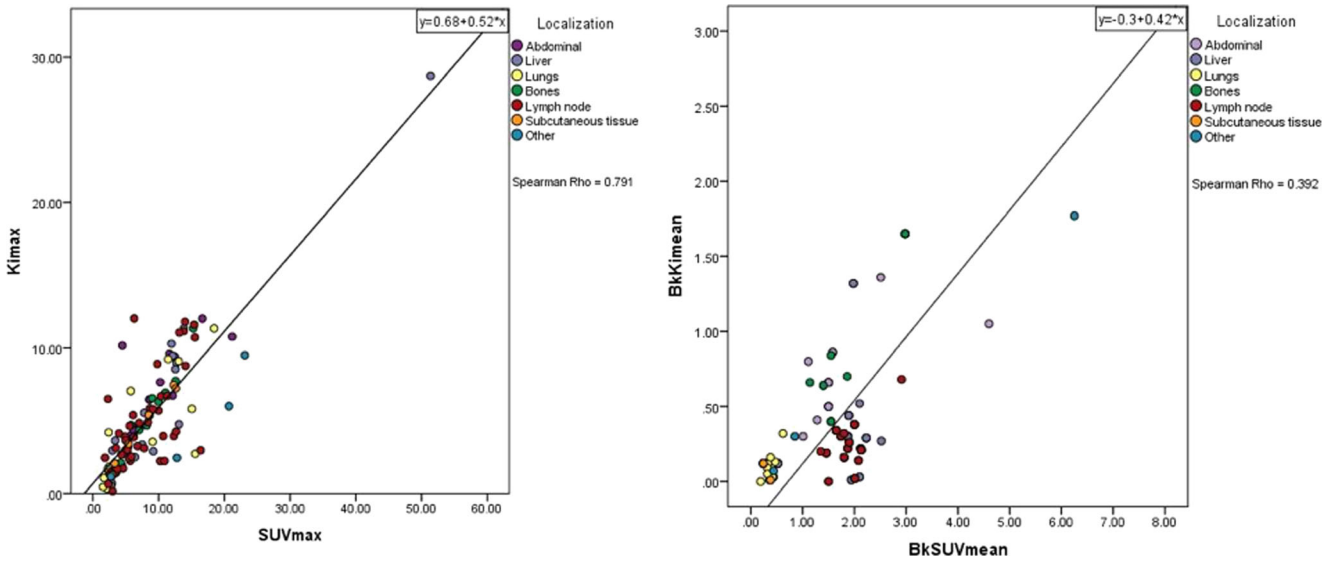

Fig. 6 Correlation plots between SUV and K_i measures for the max values of the lesions (left panel) and the mean values of the background (right panel), for each organ

HCC (patient no. 1) appearing as non-metabolic in the SUV images and as hypermetabolic in the K_i images (Fig. 3).

However, our findings suggest that the TBR and CNR metrics may not always be sufficient for quantifying lesion detectability. However, they can both indicate ability to distinguish focal lesions from their background and draw appropriate regions of interest for further quantitative evaluations. In the case of the two hepatic lesions that were negative in both SUV and K_i images, the TBR_{SUV} were 0.41 and 0.32 whereas the respective TBR_{Ki} scores were 53.33 and 43.45, respectively. Moreover, the CNR_{SUV} values were 1.40 and 1.08 whereas the CNR_{Ki} values were 364.55 and 296.99, respectively. Despite the very high TBR and CNR scores of the K_i images, the lesions were not detected, due to the very low target lesion and nearly zero background K_i values. The same effect explains why the false-positive lung lesion was not detected on K_i images (Fig. 4).

There was one interesting case (patient no. 8) of biopsy-proved benign lung lesion which was erroneously depicted as positive in SUV images (Fig. 4). There were also several findings in the standard report of SUV images of muscle activity, inflammation, or benign lymph nodes, which were not visible on the K_i images. One example is the case of benign thoracic lymph nodes depicted on SUV images (patient no. 14) but not on K_i images (Supplementary Fig. 1). Overall, K_i images detected less false-positive and less benign lesions than SUV images, thereby improving specificity.

The most important limitation of this study is the relatively low number of patients. Nevertheless, we identified a large number of oncologic lesions with large histologic diversity to form a large variety of malignancies in order to drive useful conclusions for the clinical performance assessment of WB Patlak K_i ^{18}F-FDG PET imaging. Moreover, having neglected the k_4 parameter during the Patlak analysis may have resulted in quantification errors, but only in the few regions, such as the liver or specific malignant tumors where non-negligible ^{18}F-FDG uptake reversibility was expected. Furthermore, the manual ROI drawing for the IDIF calculation is user-dependent and can be subject to variability, although the net effect on the robust Patlak analysis was non-significant.

Although the proposed protocol requires approximately 50 min of patient's involvement time, compared to 80 min for a standard SUV examination, the patient has to lie on the table during the whole 50-min examination. This may be challenging for patients and can impact throughput in clinical routine. We plan to continue this work with a prospective controlled study of a larger cohort targeting specific tumor types.

Acknowledgments This work was supported by the Swiss National Science Foundation under grant SNFN 320030_176052 and the Swiss Cancer Research Foundation under Grant KFS-3855-02-2016.

Funding This study has received funding by the Swiss National Science Foundation.

Compliance with ethical standards

Guarantor The scientific guarantor of this publication is Prof. Habib Zaidi.

Conflict of interest The authors of this manuscript declare no relationships with any companies whose products or services may be related to the subject matter of the article.

Statistics and biometry No complex statistical methods were necessary for this paper.

Informed consent Written informed consent was obtained from all subjects (patients) in this study.

Ethical approval Institutional Review Board approval was obtained.

Methodology
- prospective
- observational
- performed at one institution

References

1. Gambhir SS (2002) Molecular imaging of cancer with positron emission tomography. Nat Rev Cancer 2:683–693
2. Czernin J, Allen-Auerbach M, Schelbert HR (2007) Improvements in cancer staging with PET/CT: literature-based evidence as of September 2006. J Nucl Med 48:78S–788S
3. Huang SC (2000) Anatomy of SUV. Standardized uptake value. Nucl Med Biol 27:643–646
4. Boellaard R (2011) Need for standardization of 18F-FDG PET/CT for treatment response assessments. J Nucl Med 52(Suppl 2):93S–100S
5. Zaidi H, Karakatsanis N (2018) Towards enhanced PET quantification in clinical oncology. Br J Radiol 91:20170508
6. Strauss LG, Klippel S, Pan L, Schonleben K, Haberkorn U, Dimitrakopoulou-Strauss A (2007) Assessment of quantitative FDG PET data in primary colorectal tumours: which parameters are important with respect to tumour detection? Eur J Nucl Med Mol Imaging 34:868–877
7. Freedman NM, Sundaram SK, Kurdziel K et al (2003) Comparison of SUV and Patlak slope for monitoring of cancer therapy using serial PET scans. Eur J Nucl Med Mol Imaging 30:46–53
8. Gupta N, Gill H, Graeber G, Bishop H, Hurst J, Stephens T (1998) Dynamic positron emission tomography with F-18 fluorodeoxyglucose imaging in differentiation of benign from malignant lung/mediastinal lesions. Chest 114:1105–1111
9. Tixier F, Vriens D, Cheze-Le Rest C et al (2016) Comparison of tumor uptake heterogeneity characterization between static and parametric 18F-FDG PET images in non-small cell lung cancer. J Nucl Med 57:1033–1039
10. Wang G, Qi J (2013) Direct estimation of kinetic parametric images for dynamic PET. Theranostics 3:802–815
11. Veronese M, Rizzo G, Bertoldo A, Turkheimer FE (2016) Spectral analysis of dynamic PET studies: a review of 20 years of method developments and applications. Comput Math Methods Med 2016: 7187541
12. Kotasidis F, Tsoumpas C, Rahmim A (2014) Advanced kinetic modelling strategies: towards adoption in clinical PET imaging. Clin Transl Imaging 2:219–237
13. Zhang J, Wang R, Fan Y et al (2017) Application of quantitative dynamic whole-body 18FDG-PET/CT in the differential diagnosis of pulmonary nodules [abstract]. J Nucl Med 58:86
14. Epelbaum R, Frenkel A, Haddad R et al (2013) Tumor aggressiveness and patient outcome in cancer of the pancreas assessed by dynamic 18F-FDG PET/CT. J Nucl Med 54:12–18
15. Strauss LG, Koczan D, Klippel S et al (2013) Dynamic PET with (18)F-Deoxyglucose (FDG) and quantitative assessment with a two-tissue compartment model reflect the activity of glucose transporters and hexokinases in patients with colorectal tumors. Am J Nucl Med Mol Imaging 3:417–424
16. Wangerin KA, Muzi M, Peterson LM et al (2017) A virtual clinical trial comparing static versus dynamic PET imaging in measuring response to breast cancer therapy. Phys Med Biol 62:3639–3655
17. Patlak CS, Blasberg RG (1985) Graphical evaluation of blood-to-brain transfer constants from multiple-time uptake data. Generalizations. J Cereb Blood Flow Metab 5:584–590
18. Slifstein M, Laruelle M (2001) Models and methods for derivation of in vivo neuroreceptor parameters with PET and SPECT reversible radiotracers. Nucl Med Biol 28:595–608
19. Bentourkia M, Zaidi H (2007) Tracer kinetic modeling in PET. PET Clin 2:267–277
20. Rahmim A, Lodge MA, Karakatsanis NA et al (2018) Dynamic whole-body PET imaging: principles, potentials and applications. Eur J Nucl Med Mol Imaging (in press). https://doi.org/10.1007/s00259-018-4153-6
21. Jakoby BW, Bercier Y, Watson CA, Bendriem B, Townsend DW (2009) Performance characteristics of a new LSO PET/CT scanner with extended axial field-of-view and PSF reconstruction. IEEE Trans Nucl Sci 56:633–639
22. Surti S (2015) Update on time-of-flight PET imaging. J Nucl Med 56:98–105
23. Rahmim A, Qi J, Sossi V (2013) Resolution modeling in PET imaging: theory, practice, benefits, and pitfalls. Med Phys 40: 064301–064315
24. Karakatsanis NA, Lodge MA, Tahari AK, Zhou Y, Wahl RL, Rahmim A (2013) Dynamic whole-body PET parametric imaging: I. Concept, acquisition protocol optimization and clinical application. Phys Med Biol 58:7391–7418
25. Karakatsanis NA, Lodge MA, Zhou Y, Wahl RL, Rahmim A (2013) Dynamic whole-body PET parametric imaging: II. Task-oriented statistical estimation. Phys Med Biol 58:7419–7445
26. Karakatsanis NA, Zhou Y, Lodge MA et al (2015) Generalized whole-body Patlak parametric imaging for enhanced quantification in clinical PET. Phys Med Biol 60:8643–8673
27. Karakatsanis NA, Casey ME, Lodge MA, Rahmim A, Zaidi H (2016) Whole-body direct 4D parametric PET imaging employing nested generalized Patlak expectation-maximization reconstruction. Phys Med Biol 61:5456–5485
28. Zhu W, Li Q, Bai B, Conti PS, Leahy RM (2014) Patlak image estimation from dual time-point list-mode PET data. IEEE Trans Med Imaging 33:913–924
29. Karakatsanis N, Lodge M, Zhou Y et al (2015) Novel multi-parametric SUV/Patlak FDG-PET whole-body imaging framework for routine application to clinical oncology [abstract]. J Nucl Med 56:625
30. Karakatsanis NA, Lodge MA, Rahmim A, Zaidi H (2014) Introducing time-of-flight and resolution recovery image reconstruction to whole-body PET parametric imaging. IEEE Nuclear Science Symposium and Medical Imaging Conference (NSS/MIC), Seattle, WA, 8–15 November 2014
31. Tomasi G, Kimberley S, Rosso L, Aboagye E, Turkheimer F (2012) Double-input compartmental modeling and spectral analysis for the quantification of positron emission tomography data in oncology. Phys Med Biol 57:1889–1906
32. van der Weerdt AP, Klein LJ, Boellaard R, Visser CA, Visser FC, Lammertsma AA (2001) Image-derived input functions for determination of MRGlu in cardiac (18)F-FDG PET scans. J Nucl Med 42:1622–1629
33. Zhuang M, Karakatsanis NA, Dierckx RAJO, Zaidi H (2018) Quantitative analysis of heterogeneous 18F-FDG static (SUV) vs. Patlak (Ki) whole-body PET imaging using different segmentation methods: a simulation study. Mol Imaging Biol (in press). https://doi.org/10.1007/s11307-018-1241-8
34. Dimitrakopoulou-Strauss A, Georgoulias V, Eisenhut M et al (2006) Quantitative assessment of SSTR2 expression in patients with non-small cell lung cancer using (68)Ga-DOTATOC PET and comparison with (18)F-FDG PET. Eur J Nucl Med Mol Imaging 33:823–830